Investigation of Load Sharing Factor of the Fixed-Setting Face-Milled Curvilinear Cylindrical Gear by Finite Element Method

Xuegang Zhang[1,*], Yingjie Dong[2] and Bin Gan[3]

[1] School of Intelligent Manufacturing, Panzhihua University, Panzhihua, 617000, China

[2] Panzhihua Hangyu New Material Technology Co., Ltd., Panzhihua, 617000, China

[3] Sichuan Provincial Key Lab of Process Equipment and Control, Sichuan University of Science & Engineering, Zigong, 643002, China

Revista Internacional
Métodos numéricos
para cálculo y diseño en ingeniería
RIMNI
UNIVERSITAT POLITÈCNICA DE CATALUNYA BARCELONATECH
In cooperation with CIMNE

INFORMATION

Keywords:
Curvilinear cylindrical gears
element sensitivity analysis
finite element method
hertz theory
load sharing factor

DOI: 10.23967/j.rimni.2024.10.57217

SCIPEDIA Revista Internacional de Métodos Numéricos para Cálculo y Diseño en Ingeniería

RIMNI

Investigation of Load Sharing Factor of the Fixed-Setting Face-Milled Curvilinear Cylindrical Gear by Finite Element Method

Xuegang Zhang[1,*], **Yingjie Dong**[2] **and Bin Gan**[3]

[1]School of Intelligent Manufacturing, Panzhihua University, Panzhihua, 617000, China

[2]Panzhihua Hangyu New Material Technology Co., Ltd., Panzhihua, 617000, China

[3]Sichuan Provincial Key Lab of Process Equipment and Control, Sichuan University of Science & Engineering, Zigong, 643002, China

ABSTRACT

The fixed-setting face-milled curvilinear cylindrical gear (FSC gear) is a type of parallel-axis gear characterized by a circular arc-shape tooth in the longitudinal direction, with contact impressions on the tooth surface that can be adjusted through the manufacturing process. The finite element method is employed to investigate the effects of various gear parameters on the load-sharing factor (LSF) of FSC-gears. Initially, a sensitivity analysis was conducted to enhance the accuracy of the finite element model for FSC gear drives. Secondly, the accuracy of the finite element model was validated by the Hertzian contact theory. Furthermore, the correctness of the finite element method for determining the LSF was validated based on American Gear Manufacturers Association standards (AGMA). In this study, the effects of assembly errors, tooth modification, driving torque, cutter radius, and contact pattern size on LSF are investigated by numerical examples. The results show that the precise LSF can be determined without intentionally increasing the element density of the subsurface of the tooth surface. Compared with the AGMA standard, the finite element method offers advantages in calculating the LSF of any non-standard gear. The influence of the milling cutter radius and the tooth surface contact pattern size on the LSF can be neglected.

OPEN ACCESS

Received: 11/08/2024

Accepted: 21/11/2024

Published: 07/04/2025

DOI
10.23967/j.rimni.2024.10.57217

Keywords:
Curvilinear cylindrical gears
element sensitivity analysis
finite element method
hertz theory
load sharing factor

1 Introduction

The fixed-setting face-milling method is one of several techniques used for machining bevel gears. This method allows for the adjustment of the contact pattern on the tooth surface, thereby improving the meshing performance of bevel gear drives [1,2]. The basic principle involves processing the pinion with a double-edged face milling cutter that has a specific curvature radius, while the concave and convex surfaces of the wheel are machined using two different radius single-edged face milling cutters. The curvature radius of the single-edged face milling cutter is determined based on the desired size of the contact pattern. The difficulty of this processing method lies in the need to reverse-calculate the

*Correspondence: Xuegang Zhang (xuegang.zhang@yahoo.com).

radius of the single-edged cutter based on the required contact pattern size in advance; otherwise, the desired contact effect cannot be achieved [3]. In our previous research [4,5], this machining technique was applied to curvilinear cylindrical gears, resulting in the development of the fixed-setting face-milled curvilinear cylindrical gear (FSC-gear). The FSC-gear drive enables adjustment of the tooth surface contact pattern using specially designed single-edged cutters.

Related studies on the problem of load sharing can be traced back to the 1970s [6–9]. Most of this research relies on mechanical principles to provide approximate estimations [10]. These studies primarily employ the boundary element method [11], the minimum elastic potential energy method [12], and the finite element method [13,14]. Each method has its own limitations, and most are applied to standard spur and helical gears [15–17]. With advancements in science and technology, many scholars have recently applied these methods to more complex gear drives. Rama [18] studied the load sharing of spur gears with tooth root cracks using the finite element method. Wei et al. [19] investigated the load sharing of helical gears with flank deviations through finite element analysis. Sancgez et al. [20] improved the minimum potential energy method for non-standard spur and helical gears. Peng et al. [12] examined the load sharing factor (LSF) of helical gears with tooth surface modifications and assembly errors by utilizing the minimum potential energy method. Chen et al. [21] explored the wear problem of spur gears based on an improved load share model. Zhang et al. [22] proposed a load distribution calculation method that combines a tooth contact mechanics model with the finite element method, which was used to study the contact problems in harmonic and planetary gears [23]. Lu et al. [24] investigated the calculation of the LSF of spur gears under thermal elastohydrodynamic lubrication. Zhang et al. [25] proposed a tooth surface partition method to calculate the LSF of spiral bevel gears, and validating the method with the potential energy method. Wu et al. [26] examined the load sharing of curvilinear cylindrical gears using load tooth contact analysis (LTCA), focusing on the influence of cutter radius, torque, and other factors on the LSF.

The FCS gear is a novel type of gear characterized by a complex tooth profile and operating conditions, which renders existing LSF models inadequate for solving the LSF problem associated with this gear. This study employs the finite element method (FEM) to investigate the LSF of FCS gears. The primary contributions of this work are as follows: (1) An examination of the independence of structured elements within the gear finite element model; (2) Validation of the accuracy of the finite element model using Hertzian contact theory; (3) Utilization of the trapezoidal method as a post-processing tool for finite element analysis results, enabling the automatic calculation of the gear's LSF, with verification of its correctness against AGMA standards; and (4) A detailed investigation into the individual effects of various factors on the LSF, including gear assembly errors, tooth surface modifications, driving torque, and face-milled cutter radius.

2 Element Sensitivity Analysis for FEM

The number of nodes and elements, and local element refinement in the FEM has a significant impact on the accuracy of simulation results. Balancing calculation time and solution accuracy is a crucial consideration in finite element analysis. According to the FEM for gear teeth proposed by Litvin et al. [27], the number and density of tooth elements are primarily determined by five parameters: the element refinement case of the subsurface of the tooth surface (N_c), the number of nodes in the longitudinal direction (N_l), the number of nodes in the tooth profile (N_p), the number of nodes in the tooth root (N_f), and the number of nodes in the geared ring (N_r). The definitions of these parameters are illustrated in Fig. 1a. Since only the tooth surfaces of two gears are in contact during

operation. So, the element sensitivity analysis focuses mainly on the three parameters: N_c, N_p, and N_l. The parameter N_c is divided into three cases: Case (I), Case (II), Case (III), as shown in Fig. 1b.

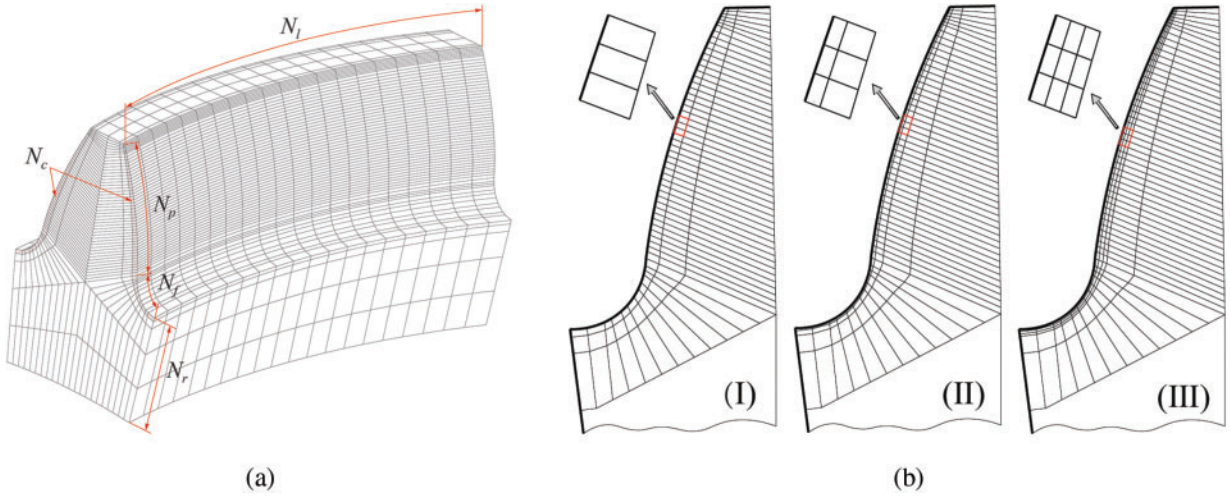

Figure 1: The definition diagram of the number of nodes in the FEM. (a) Definition of node and element numbers of single tooth model; (b) definition of the element refinement case of the subsurface of the tooth surface

The gear drive parameters listed in Table 1 are used for the element sensitivity analysis. Additionally, the radius of the double-edged cutter is set to $R = 60$ mm, the radius of the inner blade cutter is $r_{ib} = 56.8584$ mm, and the radius of the outer blade cutter is $r_{ob} = 63.1416$ mm. The applied driving torque is $T = 150$ N·m. To achieve more rigorous results, it is necessary to observe the maximum contact stress on the gear tooth surface over a meshing cycle. The meshing process within one cycle is discretized into 21 contact points to optimize the balance between solution accuracy and computation time. The construction method for the FEM of the gear drive is detailed in Reference [2].

Table 1: Basic parameters of gear drives

Parameter	Values
Number of teeth	31/40
Module (mm)	4
Normal pressure angle	20
Addendum coefficient	1
Dedendum coefficient	1.25
Face width (mm)	30
Fillet radius coefficient	0.38
Young's modulus (MPa)	2.08×10^5
Poisson's ratio	0.298

(1) The element sensitivity of parameter N_p in the tooth profile direction was analyzed. The values of N_p considered were 40, 50, 60, 70, and 100, with $N_l = 40$, $N_c = 6$, $N_f = 11$, and $N_r = 5$ held constant. The results of these FEMs are presented in Fig. 2. When $N_p \geq 50$, the contact stresses on the

tooth surface in the smooth meshing area (this area is defined as the region outside of when the teeth are just entering and just exiting engagement.) tend to stabilize. Therefore, $N_p = 50$ is deemed more appropriate.

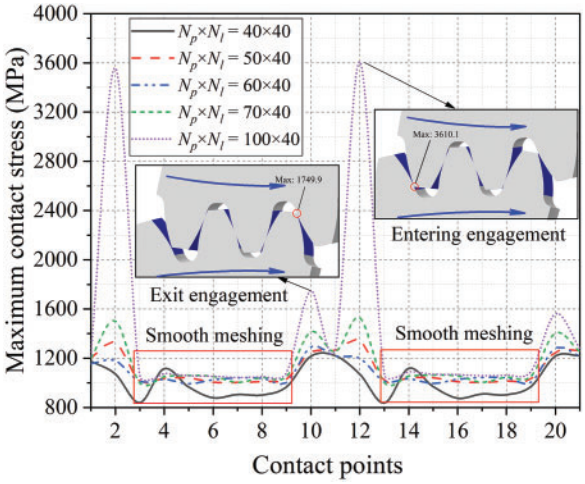

Figure 2: Evolution of the maximum contact stresses under different N_p values

(2) The element sensitivity of parameter N_l in the longitudinal direction was analyzed. The values of N_l considered were 20, 30, 40, 50, 60, and 70, with $N_p = 40$ held constant. The results of these FEMs simulations are presented in Fig. 3. When $N_l \geq 40$, the contact stresses on the tooth surface tend to stabilize. Consequently, $N_l = 40$ is considered optimal.

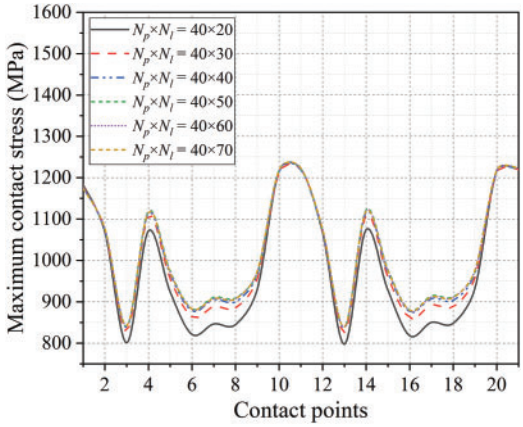

Figure 3: Evolution of the maximum contact stresses under different N_l values

(3) The element sensitivity of the element refinement case was analyzed. Assuming $N_p \times N_l = 40 \times 70$, the element refinement of the subsurface of the tooth surface was examined in three cases as depicted in Fig. 1b. The results, shown in Fig. 4, indicate that N_c has minimal impact on the maximum contact stress. Therefore, 'Case (I)' from Fig. 1b is selected as the FEM. It is concluded that there is no need to further refine element of the tooth surface elements.

In summary, the number of nodes in the FEM is set to $N_p \times N_l = 50 \times 40$, with the node distribution in the tooth thickness following 'Case (I)'. In this paper, N_f is set to 6 and N_r is set to

5. The definition of the element number of the tooth root and geared rim parts follow the method in Reference [27].

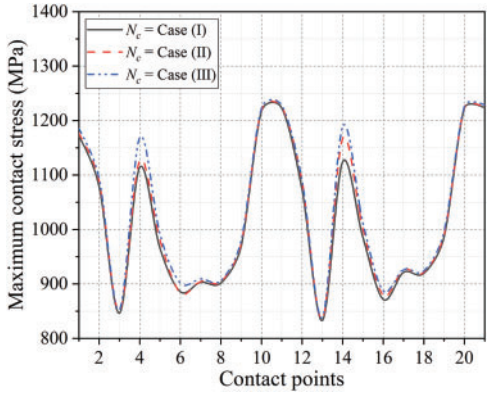

Figure 4: Evolution of the maximum contact stresses under different cases

3 Verification of FEM

In this section, Hertz contact theory is employed to verify the accuracy of the FEM. In Fig. 5, the principal curvatures of surface $\sum_1$ are $R_x^{(1)}$ and $R_y^{(1)}$, while those of surface $\sum_2$ are $R_x^{(2)}$ and $R_y^{(2)}$. These surfaces come into contact at point 'O' under the normal external force F_n. Due to the elastic deformation of the materials, a contact ellipse much smaller than the radii of the objects forms at the contact point 'O'. The dimensions of the contact ellipse are represented by the parameters a and b. The amount of contact deformation is expressed by the parameter δ_c, and the maximum contact pressure is denoted by P_{max}. The pressure distribution along the major and minor axes of the contact ellipse is described by the parameters P(x) and P(y), respectively. The parameter γ represents the misalignment angle between the principal curvatures of the two surfaces.

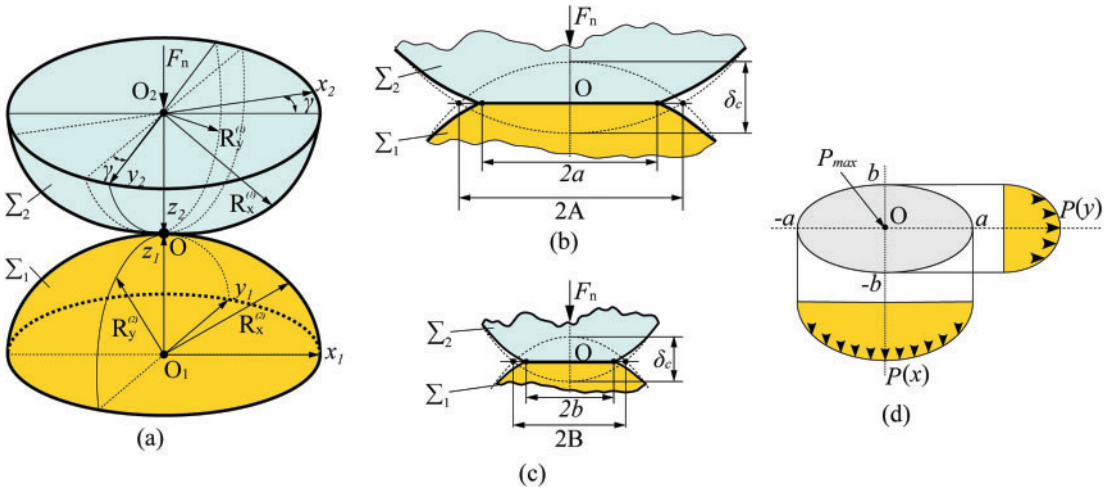

Figure 5: Definition of contact parameters. (a) 3D contact model; (b) x-z plane; (c) y-z plane; (d) pressure distribution on the contact ellipse

If the deformation and interference caused by the contact between two surfaces are not considered, the intersection line formed by the two surfaces would create a contact ellipse. The lengths of the major and minor axes of the contact ellipse are denoted by symbols A and B, respectively, and these parameters satisfy Eq. (1) [28].

$$\begin{cases} A+B=\dfrac{1}{2}\left(\dfrac{1}{R_x^{(1)}}+\dfrac{1}{R_y^{(1)}}+\dfrac{1}{R_x^{(2)}}+\dfrac{1}{R_y^{(2)}}\right) \\ B-A=\dfrac{1}{2}\left[\left(\dfrac{1}{R_x^{(1)}}-\dfrac{1}{R_y^{(1)}}\right)^2+\left(\dfrac{1}{R_x^{(2)}}-\dfrac{1}{R_y^{(2)}}\right)^2+2\left(\dfrac{1}{R_x^{(1)}}-\dfrac{1}{R_y^{(1)}}\right)\left(\dfrac{1}{R_x^{(2)}}-\dfrac{1}{R_y^{(2)}}\right)\cos(2\gamma)\right]^{1/2} \end{cases} \tag{1}$$

When considering the interference and deformation of the two surfaces, the dimensions of the contact ellipse, denoted as symbols a and b, can be determined using Eq. (2) [28].

$$\begin{cases} a=k_a\left[\dfrac{3F_n}{2E^*(A+B)}\right]^{1/3} \\ b=k_b\left[\dfrac{3F_n}{2E^*(A+B)}\right]^{1/3} \end{cases} \tag{2}$$

Here, the symbol E^* denotes the equivalent elastic modulus.

The equivalent elastic modulus can be calculated by Eq. (3).

$$\frac{2}{E^*}=\frac{1-v_1^2}{E_1}+\frac{1-v_2^2}{E_2} \tag{3}$$

Here, symbols v_1 and v_1 denote the Poisson's ratios of $\sum_1$ and $\sum_2$, respectively. Symbols E_1 and E_2 denote the elastic moduli of contact bodies $\sum_1$ and $\sum_2$, respectively. Symbols k_a and k_b in Eq. (2) can be determined using Eq. (4) [29].

$$\begin{cases} k_a=\left(\dfrac{2E(e)}{\pi(1-e^2)}\right)^{\frac{1}{3}} \\ k_b=k_a\sqrt{1-e^2} \end{cases} \tag{4}$$

Here, symbol e denotes the eccentricity of contact ellipse, it can be calculated by Eq. (5).

$$e=\sqrt{1-\frac{b^2}{a^2}} \tag{5}$$

Here, symbol $E(e)$ denotes the complete elliptic integral of the second kind, it can be calculated by Eq. (6).

$$E(e)=\int_0^{\frac{\pi}{2}}\sqrt{1-e^2\sin^2\alpha}\,\mathrm{d}\alpha \tag{6}$$

The eccentricity e satisfies not only Eq. (4) but also Eq. (7) [30].

$$\frac{|B-A|}{|A+B|}=\frac{2(1-e^2)}{e^2}\frac{E(e)-K(e)}{K(e)}+1=\cos\theta \tag{7}$$

Here, symbol θ denotes the angle in range 0 to π. Symbol $K(e)$ represents the complete elliptic integral of the first kind, which can be calculated using Eq. (8).

$$K(e) = \int_0^{\frac{\pi}{2}} \frac{1}{\sqrt{1 - e^2 \sin^2 \alpha}} d\alpha \tag{8}$$

According to Eq. (7), the elliptic eccentricity e can be solved using the Newton method. Once e is determined, it can be substituted into Eqs. (2) to (4) to solve for the contact ellipse dimensions a and b.

In this study, the ratio a/b is very large, which results in the elliptic eccentricity e being close to 1. Consequently, the parameter $K(e)$ approaches infinity, while the parameter $E(e)$ approaches 1, as shown in Fig. 6. When using the Newton iteration method to solve Eq. (7), selecting an appropriate initial value for the elliptic eccentricity e is crucial, as an incorrect initial value may prevent the calculation from converging. After repeated trials, the initial iteration value $e_0 = 0.999999$ was chosen for this study.

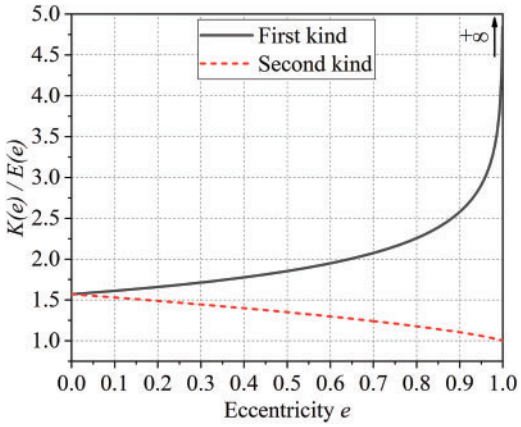

Figure 6: First and second kind of elliptic integrals corresponding to the eccentricity

Fig. 6 illustrates the relationship between two types of complete elliptic integrals and the elliptical eccentricity. The elastic deformation resulting from the contact can be expressed by Eq. (9) [31].

$$\delta_c = \frac{3}{2} \frac{F_n b K(e)}{\pi a b} \frac{1}{E^*} \tag{9}$$

The maximum contact pressure can be calculated by Eq. (10) [31].

$$P_{\max} = \frac{3}{2} \frac{F_n}{\pi a b} \tag{10}$$

As shown in Fig. 5d, the pressure distribution along the major and minor axes of the contact ellipse can be described by Eqs. (11) and (12), respectively [31].

$$P(x) = P_{\max} \sqrt{1 - \left(\frac{x}{a}\right)^2} \quad (-a \le x \le a) \tag{11}$$

$$P(y) = P_{\max} \sqrt{1 - \left(\frac{y}{b}\right)^2} \quad (-b \le x \le b) \tag{12}$$

Then, the contact pressure distribution on the contact elliptic is [31]:

$$P = P_{\max}\sqrt{1-\left(\frac{x^2}{a^2}+\frac{y^2}{b^2}\right)} \quad (-a \le x \le a, -b \le x \le b) \tag{13}$$

In this section, the FEM is validated using the gear parameters listed in Table 1. The stress distribution at a specific contact point is employed to verify the accuracy of the FEM. Specifically, the 11th contact point during single-tooth meshing is compared with the Hertz contact model. The contact pressure distribution on the tooth surface is calculated using both the FEM and the Hertz model, as shown in Fig. 7. The results indicate that the maximum contact pressure obtained from the FEM is 1266.15 MPa, while that from the Hertz model is 1230.24 MPa, resulting in a maximum contact pressure deviation of 2.84%. The length of the major axis of the contact ellipse obtained from the finite element model is slightly larger than that of the Hertz model, as shown in Fig. 7c. The length of the minor axis of the contact ellipse from the finite element model is essentially equivalent to that of the Hertz model, as shown in Fig. 7d. This discrepancy is attributed to the mesh density on the tooth surface in the finite element model. Overall, the two results show good consistency in contact pressure on the tooth surface at the 11th contact position.

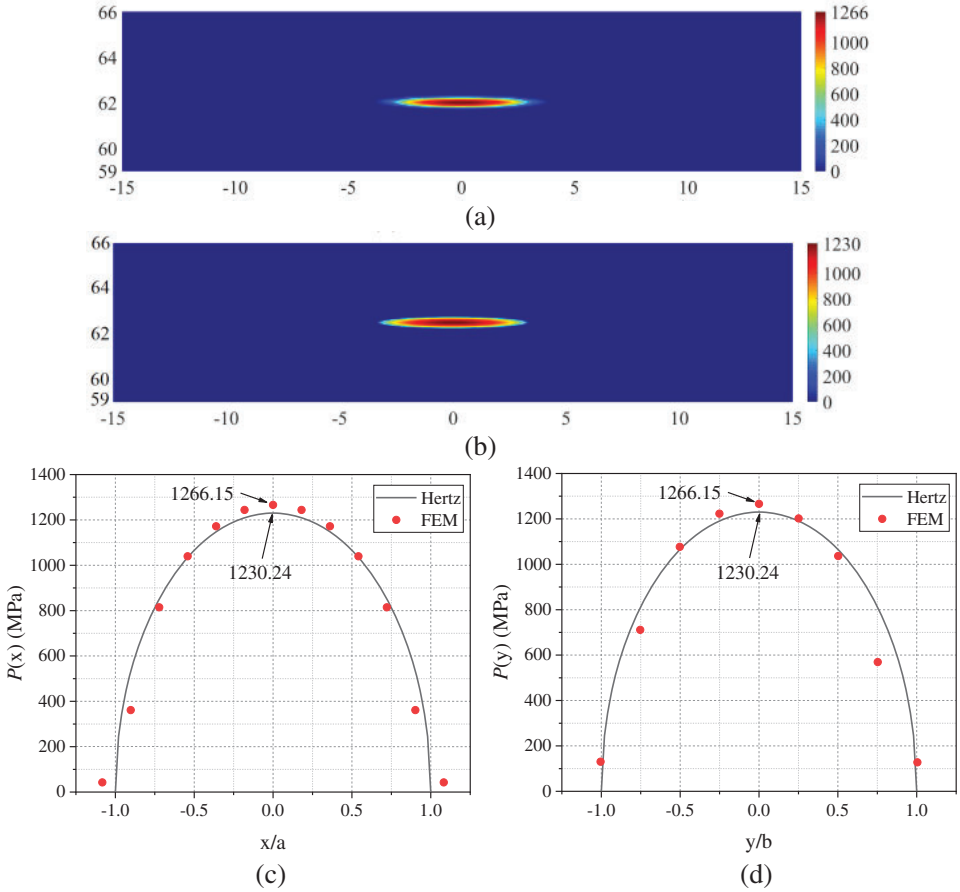

Figure 7: Contact pressure distribution on the tooth surface. (a) FEM model; (b) Hertz model; (c) major axis; (d) minor axis

Fig. 8 illustrates the evolution of the maximum contact pressure on the tooth surface during the meshing period when multiple teeth are engaged simultaneously. Due to the presence of tooth tip-edge contact when the tooth surface enters and exits the meshing, severe contact pressure is generated at contact points 2 and 20 in the FEM. However, these edge contact cannot be validated by Hertzian theory. The deviation of the maximum contact pressure at the effective contact points (3∼19) was compared. The diagram shows that the results obtained using Hertzian theory are slightly lower than those from the FEM, with a deviation of 3.1% (the maximum deviation of all contact points.) over the entire meshing cycle. Therefore, the FEM used in this study is suitable for analyzing tooth surface stress and calculating the LSF.

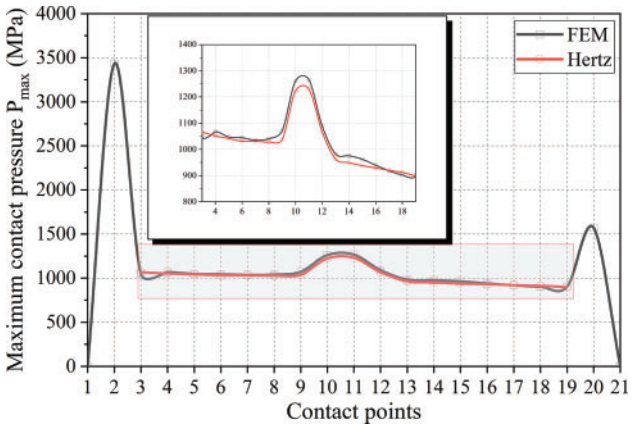

Figure 8: The evolution of maximum contact pressure on the tooth surface during the meshing cycle

4 The Solution Method for LSF

During the meshing process of the gear drive, the contact pressure at any point on the tooth surface can be expressed as a function $P(u, v)$, where the symbol u represents the coordinate value in the longitudinal direction and symbol v represents the coordinate value in the tooth profile direction. If a coordinate system is established in the normal direction to the tooth surface, the contact pressure distribution $P(v)$ in the longitudinal direction can be expressed within this coordinate system. Similarly, the stress distribution in the tooth profile direction can be expressed as $P(u)$. Both functions represent the unit load on the tooth surface, measured in N/mm. By solving the FEM of the gear drive, the contact pressure values at all nodes on the tooth surface can be obtained, with the pressure at each node expressed as $P(u, v)$, as shown in Fig. 9.

After solving the FEM, the pressure values at the tooth surface nodes are obtained as a series of discrete values. These values can be integrated using the trapezoidal rule. The total stress in the tooth profile direction is approximated by Eq. (14).

$$P(u) \simeq \sum_{u=1,v}^{k} \left[|\mathbf{r}_v^{u+1} - \mathbf{r}_v^u| \cdot \frac{p_v^{u+1} + p_v^u}{2} \right] \tag{14}$$

Here, vector symbol $\mathbf{r}$ represents the position vector of the node, and symbol p represents the pressure at the node. The superscript u indicates the row in which the node is located, where $u = 1, 2, 3, \ldots, k$. The subscript v indicates the column, where $v = 1, 2, 3, \ldots, l$. Symbol k is the total number of rows of tooth surface nodes, and symbol l is the total number of columns of tooth surface nodes.

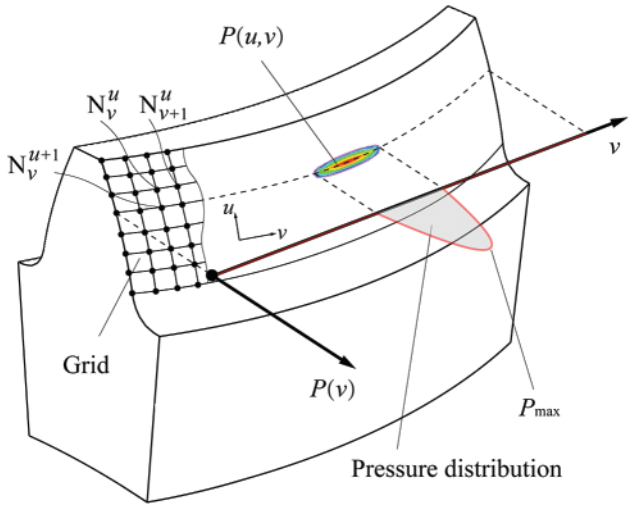

Figure 9: Explanation of contact pressure and nodes on the tooth surface

If the equivalent normal load on the tooth surface at the i-th contact point is F_{ni}, the trapezoidal rule can be used to approximate the unit load in the longitudinal direction.

$$F_{ni} \simeq \sum_{v=1,u}^{l} \left[|\mathbf{r}_{v+1}^{u} - \mathbf{r}_{v}^{u}| \cdot \frac{P_{v+1}^{u} + P_{v}^{u}}{2} \right] \tag{15}$$

The total normal load on all tooth surfaces can be solved by Eq. (16).

$$F_{nT} = \sum_{i=1}^{u} F_{ni} \tag{16}$$

The LSF on a specific tooth at the i-th contact point is defined as:

$$LSF_i = \frac{F_{ni}}{F_{nT}} \tag{17}$$

According to the AGMA standard, the LSF of spur gears can be calculated according to Eq. (18).

$$LSF\,(\theta) = \begin{cases} \dfrac{1}{3} + \dfrac{1}{3}\dfrac{\theta}{\theta_{LPSTC}} & (\theta_{START} \le \theta \le \theta_{LPSTC}) \\ 1 & (\theta_{LPSTC} \le \theta \le \theta_{HPSTC}) \\ \dfrac{1}{3} + \dfrac{1}{3}\dfrac{(\theta_{END} - \theta_{START}) - \theta}{(\theta_{END} - \theta_{START}) - \theta_{HPSTC}} & (\theta_{HPSTC} \le \theta \le \theta_{END}) \end{cases} \tag{18}$$

Using the spur gear parameters listed in Table 1 as an example, the unknown parameters involved in Eq. (18) were solved using tooth contact analysis (TCA), yielding the following results: $\theta_{START} = -9.64°$, $\theta_{END} = 9.95°$, $\theta_{LPSTC} = -1.66°$, and $\theta_{HPSTC} = 1.97°$. The LSF obtained using the AGMA standard [32] is shown in Fig. 10 (red dotted line), while the LSF calculated by the finite element method is represented by black discrete points in Fig. 10. The results indicate that the LSF values obtained by both methods are nearly identical and closely align with the experimental results reported by Spitas et al. [33].

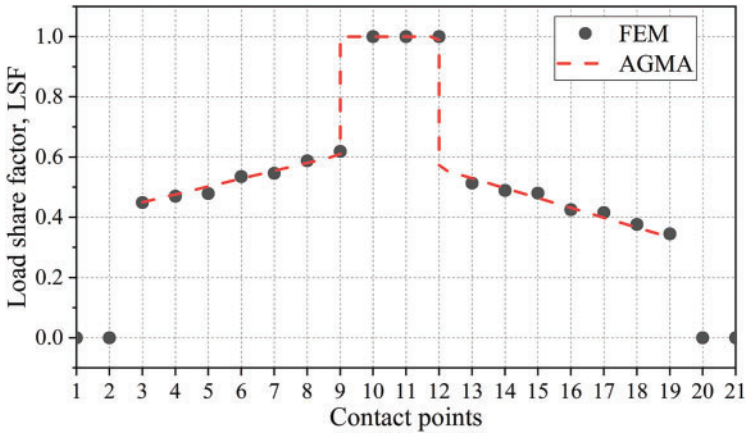

Figure 10: Comparison of LSFs solved by finite element method and AGMA standards

5 Examples

This section uses the previously proposed method to study the effects of various factors on LSF. These influencing factors include assembly errors, tooth surface displacement, resistance torque, face milling cutter radius, and the estimated contact spot ratio. All examples in this section are based on the gear parameters listed in Table 1. The radius of the double-edged cutter used for the wheel processing is denoted as R. The cutter radii for processing the convex and concave tooth surfaces of the pinion are denoted as r_{ib} and r_{ob}, respectively. The estimated contact pattern ratio (i.e., the percentage of the major axis dimension of the contact ellipse relative to the tooth width) is denoted as symbol L_c. The method for determining these parameters have been detailed in our previous work [34]. The milling cutter parameters applicable to all examples in this section are provided in Table 2.

Table 2: The face-milled cutter radius of the cutter head for the specific estimated contact pattern ratio

L_c (%)	$R = 60$ mm		$R = 80$ mm		$R = 100$ mm		$R = 120$ mm	
	r_{ib} (mm)	r_{ob} (mm)	r_{ib} (mm)	r_{ob} (mm)	r_{ib} (mm)	r_{ob} (mm)	r_{ib} (mm)	r_{ob} (mm)
100	62.9179	57.0821	82.7403	77.2597	102.5084	97.4916	122.2398	117.7602
90	62.8493	57.1507	82.6398	77.3602	102.361	97.6390	122.0304	117.9696
80	62.7728	57.2272	82.5001	77.4999	102.1559	97.8441	121.7384	118.2616
70	62.6611	57.3389	82.3060	77.6940	101.8578	98.1422	121.3152	118.6848
60	62.4867	57.5133	82.0086	77.9914	101.4021	98.5979	120.6689	119.3311
50	62.2028	57.7972	81.5196	78.4804	100.6552	99.3448	119.6122	120.3878
40	61.6870	58.3130	80.6348	79.3652	99.3086	100.6914	117.7145	122.2855

5.1 The Impact of Assembly Errors on LSF

There are four types of assembly errors in gear pairs: center distance error (ΔC), axial displacement error (ΔA), crossing shaft angle error (ΔH), and axis intersection error (ΔV) [35]. Among these four types of errors, only the crossing shaft angle error has the greatest impact on the performance of the gears [3]. Thence, this section focuses on crossing shaft angle errors, with ΔH set to 0°, 0.05°, and

0.1°. To prevent interference on the tooth surface under axis intersection error, the parameters are set as follows: $\Delta C = 0.1$ mm, $\Delta A = 0$ mm, and $\Delta V = 0°$. Additionally, the tooth surface modification coefficient (a_{pf}) is 0.0004, the resistance torque (T) is 150 N·m, the cutter radius (R) is 60 mm, the cutter radius for the convex tooth surface of the pinion (r_{ib}) is 62.2028 mm, and the cutter radius for the concave tooth surface of the pinion (r_{ob}) is 57.7972 mm, as shown in Table 2. The LSF during the meshing cycle is illustrated in Fig. 11. The gear pair engages at the 2nd contact point and disengages at the 20th contact point. The LSF at the 10th to 12th contact points is 1, indicating single-tooth engagement at these three points. Before entering single-tooth engagement, the LSF decreases with increasing ΔH; the opposite trend is observed after exiting single-tooth engagement.

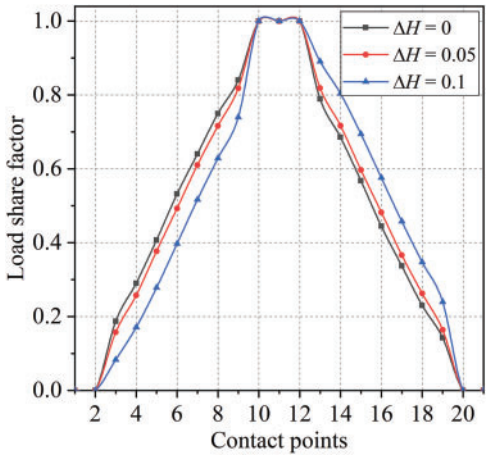

Figure 11: Evolution of the LSF for crossing shaft angle errors

Fig. 12 illustrates the stress distribution of the gear at the 11th contact point. As ΔH increases, the contact pattern (contact ellipse) on the tooth surface shifts towards the edge of tooth tip.

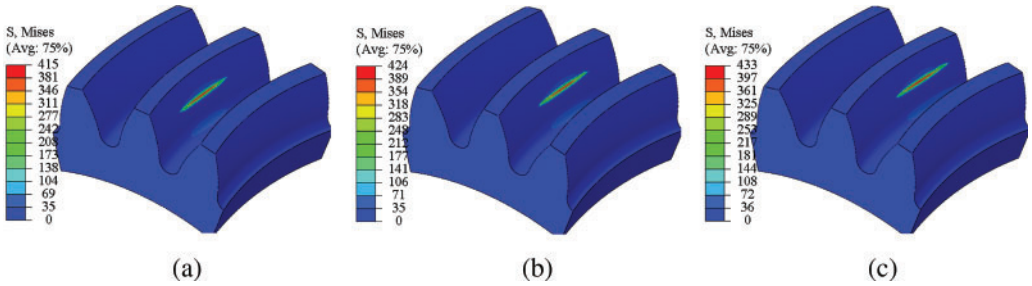

Figure 12: Stress distribution on the gear at the 11th contact point. (a) $\Delta H = 0$ mm; (b) $\Delta H = 0.05$ mm; (c) $\Delta H = 0.1$ mm

5.2 The Impact of Tooth Surface Modifications on LSF

To eliminate the harm caused by the contact of the tooth tip edges in gear transmission, parabolic tooth tip modification is introduced here. The larger the modification amount, the more material is removed from the tooth tip. Its geometric definition, please refer to Reference [3]. In this section, the tooth surface modification coefficient (a_{pf}) is set to six different values: 0, 0.0001, 0.0002, 0.0003, 0.0004, and 0.0005. The gear pair operates under ideal assembly conditions. The cutter radius (R)

is 60 mm, the cutter radius for the convex tooth surface of the pinion (r_{ib}) is 62.9179 mm, and the cutter radius for the concave tooth surface of the pinion (r_{ob}) is 57.0821 mm, as detailed in Table 2. The LSF during the meshing cycle is shown in Fig. 13. As the modification amount increases, the gear pair delays entering and advances exiting the engagement. During the initial entry and final exit of the gear teeth from engagement, the LSF decreases with an increase in the tooth surface modification amount. However, during other periods of meshing, the LSF increases as the tooth surface modification amount increases. Additionally, the single-tooth engagement period extends with greater modification amounts.

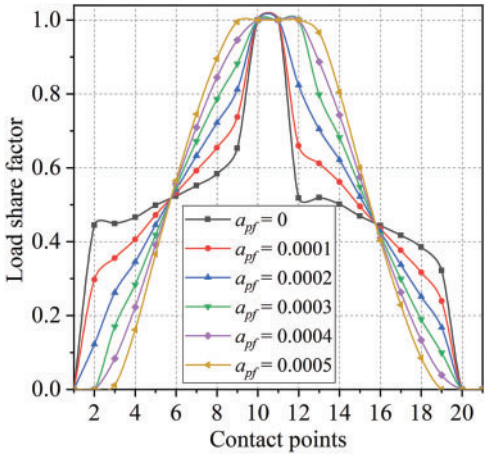

Figure 13: Evolution of the LSF for gear surface modification amounts

Fig. 14 shows the stress distribution diagram of the gear at the 19th contact point. The stress on the middle tooth decreases as the modification amount increases until the stress at the tooth tip disappears. At this contact point, the current tooth disengages from the gear drive, and the load transfers to the next tooth in the gear.

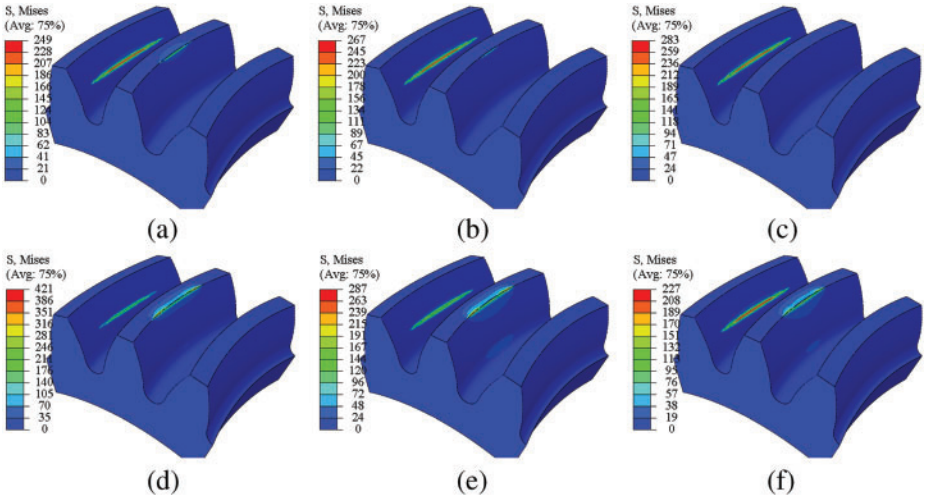

Figure 14: Stress distribution on the gear at the 19th contact point. (a) $a_{pf} = 0$; (b) $a_{pf} = 0.0001$; (c) $a_{pf} = 0.0002$; (d) $a_{pf} = 0.0003$; (e) $a_{pf} = 0.0004$; (f) $a_{pf} = 0.0005$

5.3 The Impact of Driving Torque on LSF

In this section, the driving torque (T) of the gear pair is set to four different values: 50, 100, 150, and 200 N·m. The gear pair is assumed to be under ideal assembly conditions, with a tooth surface modification coefficient (a_{pf}) of 0.0004. The cutter radius (R) is 60 mm, while the cutter radius for the convex tooth surface of the pinion (r_{ib}) is 62.4867 mm, and the cutter radius for the concave tooth surface of the pinion (r_{ob}) is 57.5133 mm, as shown in Table 2. The LSF during the meshing cycle is illustrated in Fig. 15. As the torque increases, the gear pair slightly advances in the timing of engagement and disengagement. When the gear teeth are just entering or about to exit engagement, the LSF increases with the rise in torque. During other phases of the meshing cycle, the LSF decreases as torque increases. Additionally, the single-tooth engagement period shortens with the increase in torque.

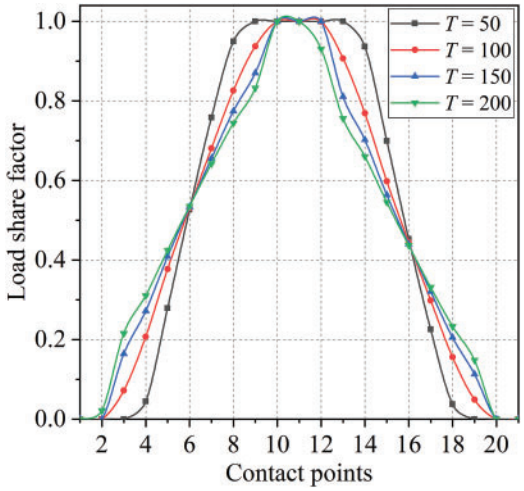

Figure 15: Evolution of the LSF for driving torques

Fig. 16 shows the stress diagram of the gear at the 12th contact point. The stress on the gear tooth decreases with the increase in torque, while the contact pattern size on the gear tooth increases with the increase in torque.

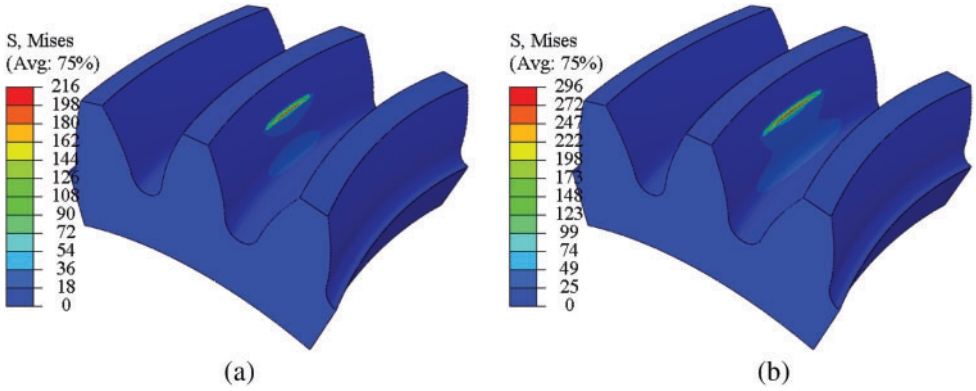

Figure 16: (Continued)

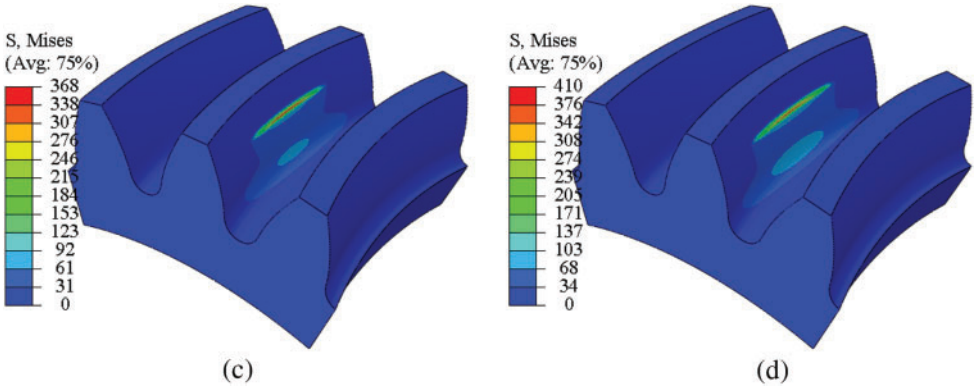

Figure 16: Stress distribution on the gear at the 12th contact point. (a) $T = 50$ N·m; (b) $T = 100$ N·m; (c) $T = 150$ N·m; (d) $T = 200$ N·m

5.4 The Impact of Cutter Radii on LSF

The double-edged cutter radius (R) for processing the wheel was set to 60, 80, 100, and 120 mm, respectively. The gear pair operates under ideal assembly conditions with a tooth surface contact pattern ratio (L_c) of 100%, a tooth surface modification coefficient (a_{pf}) of 0.0004, and an applied torque (T) of 150 N·m. The LSF during the meshing cycle is illustrated in Fig. 17. When the estimated contact pattern ratio on the tooth surface is consistent, the LSF of the gear pair remains almost identical.

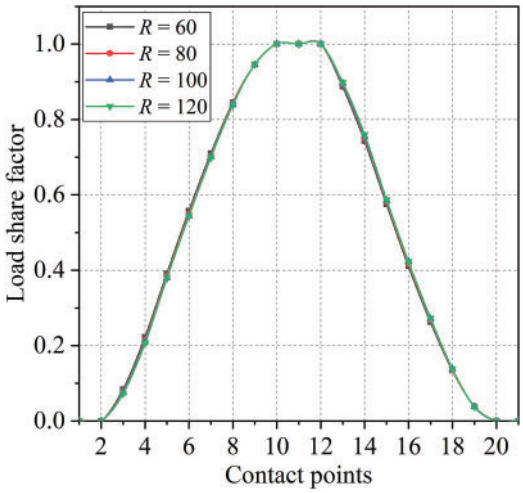

Figure 17: Evolution of the LSF for double-edged cutter radii

5.5 The Impact of Tooth Surface Contact Patterns on LSF

There is a direct relationship between the tooth surface contact pattern ratio and the curvature radius of the single-edged cutter. The specific numerical relationship is shown in Table 2. Here, the tooth surface contact pattern ratio is taken as the research object. The tooth surface contact pattern ratio (L_c) is set to 40%, 50%, 60%, 70%, 80%, 90%, and 100%, respectively. The gear pair is assumed to be under ideal assembly conditions, with a cutter radius (R) of 60 mm, a tooth surface modification

coefficient (a_{pf}) of 0.0004, and an applied torque (T) of 150 N·m. The LSF during the meshing cycle is depicted in Fig. 18. When the gear teeth are just entering or about to exit engagement, the LSF decreases as the contact pattern ratio increases. During the other phases of meshing, the LSF increases with the contact pattern ratio. However, the magnitude of these changes remains relatively small.

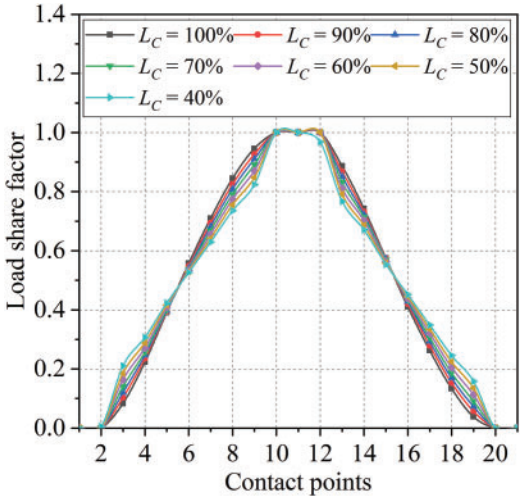

Figure 18: Evolution of the LSF for contact pattern ratios on the tooth surface

6 Conclusion

Based on the research conducted in this paper, the following conclusions can be drawn:

(1) When establishing a FEM of a gear pair to solve for contact pressure, it is generally unnecessary to excessively refine the subsurface layer elements on the tooth surface, unless subsurface stress needs to be analyzed. This is because subsurface stress is located within the gear tooth.

(2) Using FEM to calculate the LSF of gear drives is feasible. This method is applicable to non-standard gears that do not conform to AGMA standards and is particularly effective for gears with assembly errors and tooth surface modifications.

(3) The influence of cutter radius and tooth surface contact patterns on the LSF is relatively minor. Tooth surface modifications can reduce the rate of change in load sharing during the meshing cycle, thereby minimizing impact forces during gear operation. Under heavy load conditions, curvilinear cylindrical drives reduce the duration of the single-tooth engagement.

Acknowledgement: I would like to express my deepest gratitude to Professor Liang Zheng from Southwest Petroleum University, who provided the computational equipment and venue for the numerical computation part of this paper. He also offered valuable insights for the research of the text. Without his assistance, it would have been difficult to complete the research work presented in this paper.

Funding Statement: This research was supported by the Panzhihua City Provincial Targeted Financial Resources Transfer Payment (Grant No. 222Y2F-GG-04), the Sichuan Provincial Natural Science Foundation (Grant No. 2024NSFSC0140), and the Sichuan Provincial Key Lab of Process Equipment and Control (Grant No. GK202211). Additional support was provided by the Sichuan Engineering

Research Center for Titanium Alloy Advanced Manufacturing Technology (Grant No. TM-2023-Z-02), the Panzhihua Advanced Manufacturing Technology Key Laboratory (Grant No. 2022XJZD05), and the Panzhihua Science and Technology Planning Project (Grant No. 2021ZD-G-1).

Author Contributions: The authors confirm contribution to the paper as follows: study conception and design: Xuegang Zhang; data collection: Xuegang Zhang; analysis and interpretation of results: Xuegang Zhang, Yingjie Dong; draft manuscript preparation: Xuegang Zhang, Bin Gan. All authors reviewed the results and approved the final version of the manuscript.

Availability of Data and Materials: Not applicable.

Ethics Approval: Not applicable.

Conflicts of Interest: The authors declare no conflicts of interest to report regarding the present study.

References

1. Fuentes-Aznar A, Ruiz-Orzaez R, Gonzalez-Perez I. Computational approach to design face-milled spiral bevel gear drives with favorable conditions of meshing and contact. Meccanica. 2018;53(10):2669–86. doi:10.1007/s11012-018-0841-3.
2. Zhang XG, Huang XB, Gan B. Contact stresses and bending stresses analysis of curvilinear cylindrical gears generated by a face-milling cutter with parabolic profile. Revista internacional de métodos numéricos para cálculo y diseno en ingenieria. 2023;39(3):30. doi:10.23967/j.rimni.2023.09.001.
3. Gonzalez-Perez I, Fuentes-Aznar A. Conjugated action and methods for crowning in face-hobbed spiral bevel and hypoid gear drives through the spirac system. Mech Mach Theory. 2019;139:109–30. doi:10.1016/j.mechmachtheory.2019.04.011.
4. Fuentes-Aznar A, Ruiz-Orzaez R, Gonzalez-Perez I. Computerized design, simulation of meshing, and finite element analysis of two types of geometry of curvilinear cylindrical gears. Comput Methods Appl Mech Eng. 2014;272:321–39. doi:10.1016/j.cma.2013.12.017.
5. Xuegang Z, Zheng L. Geometric modeling and CFD simulation of curvilinear cylindrical gear pumps. Iran J Sci Technol Trans Mech Eng. 2023;47(1):1–17. doi:10.1007/s40997-022-00502-3.
6. Tobe T, Inoue K. Longitudinal load distribution factor of helical gears. J Mech Trans Automat Des. 1985;107(1):17–22. doi:10.1115/1.3258682.
7. Tavakoli MS, Houser DR. Optimum profile modifications for the minimization of static transmission errors of spur gears. J Mech, Trans, Automat Des. 1986;108(1):86–94. doi:10.1115/1.3260791.
8. Hayashi T, Li XY, Hayashi I, Endo K, Watanabe W. Measurement and some discussions on dynamic load sharing in planetary gears. Bull JSME. 1986;29(253):2290–7. doi:10.1299/jsme1958.29.2290.
9. Simon V. Load and stress distributions in spur and helical gears. J Mech Trans Automat Des. 1988;110(2):197–202. doi:10.1115/1.3258926.
10. Singh A. Application of a system level model to study the planetary load sharing behavior. J Mech Des. 2005;127(3):469–76. doi:10.1115/1.1864115.
11. Kanber B. Analysis of spur gears by coupling finite and boundary element methods. Mech Des Struct Mach. 2006;34(6):307–24. doi:10.1080/15397730600889498.
12. Peng Y, Zhao N, Qiu P, Zhang M, Li W, Zhou R. An efficient model of load distribution for helical gears with modification and misalignment. Mech Mach Theory. 2018;121:151–68. doi:10.1016/j.mechmachtheory.2017.10.019.

13. Atanasovska I, Mitrović R, Momčilović D, Subic A. Analysis of the nominal load effects on gear load capacity using the finite-element method. Proc Inst Mech Eng Part C: J Mech Eng Sci. 2010;224(11):2539–48. doi:10.1243/09544062JMES2508.
14. Khosroshahi MG, Fattahi AM. Three dimensional stress analysis of a helical gear drive with finite element method. Mechanika. 2017;23(5):630. doi:10.5755/j01.mech.23.5.14884.
15. Deepak D, Tamilselvam P. Theoretical and analytical research on load sharing in helical gear with evaluating the FEA method and computerized approach of AGMA standards. J Combinat Optim. 2023;45(3):87. doi:10.1007/s10878-023-01003-y.
16. Pedrero JI, Pleguezuelos M, Artés M, Antona JA. Load distribution model along the line of contact for involute external gears. Mech Mach Theory. 2010;45(5):780–94. doi:10.1016/j.mechmachtheory.2009.12.009.
17. Behvar A, Tahmasbi K, Savich W, Haghshenas M. Tooth interior fatigue fracture in automotive differential gears. Eng Fail Anal. 2024;156:107829.
18. Rama T, Gnanasekar N. Investigation of the effect of load distribution along the face width and load sharing between the pairs in contact on the fracture parameters of the spur gear tooth with root crack. Eng Fail Anal. 2019;97:518–33. doi:10.1016/j.engfailanal.2019.01.051.
19. Wei J, Sun W, Wang L. Effects of flank deviation on load distributions for helical gear. J Mech Sci Technol. 2011;25(7):1781–9. doi:10.1007/s12206-011-0416-x.
20. Sánchez MB, Pleguezuelos M, Pedrero JI. Enhanced model of load distribution along the line of contact for non-standard involute external gears. Meccanica. 2013;48(3):527–43. doi:10.1007/s11012-012-9612-8.
21. Chen Z, Ji P. Study on wear in spur gears based on an improved load distribution model considering the effects of corner contact. Eng Fail Anal. 2020;115:104605. doi:10.1016/j.engfailanal.2020.104605.
22. Zhang Y, Wang G, Pan X, Li Y. Calculating the load distribution and contact stress of the disposable harmonic drive under full load. Machines. 2022;10(2):96. doi:10.3390/machines10020096.
23. Ryali L, Talbot D. A dynamic load distribution model of planetary gear sets. Mech Mach Theory. 2021;158(3):104229. doi:10.1016/j.mechmachtheory.2020.104229.
24. Lu R, Tang W, Huang Q, Xie J. An improved load distribution model for gear transmission in thermal elastohydrodynamic lubrication. Lubricants. 2023;11(4):177. doi:10.3390/lubricants11040177.
25. Zhang Y, Zhu L, Gou X. Calculation methods of load distribution ratio for spiral bevel gear. Int J Mech Sci. 2023;257(11):108531. doi:10.1016/j.ijmecsci.2023.108531.
26. Wu Y, Luo P, Bai Q, Liang S, Fan Q, Hou Li. Modelling and analyzing of loaded meshing characteristics of cylindrical gear transmission with curvilinear-shaped teeth. Meccanica. 2023;58(8):1555–80. doi:10.1007/s11012-023-01690-1.
27. Litvin FL, Fuentes A. Gear geometry and applied theory. 2nd ed. Cambridge: Cambridge University Press; 2004.
28. Popov VL. Contact mechanics and friction. Berlin: Springer Berlin Heidelberg; 2010.
29. Yastrebov VA. Numerical methods in contact mechanics. John Wiley & Sons; 2013.
30. Gonzalez-Perez I, Iserte JL, Fuentes A. Implementation of Hertz theory and validation of a finite element model for stress analysis of gear drives with localized bearing contact. Mech Mach Theory. 2011;46(6):765–83. doi:10.1016/j.mechmachtheory.2011.01.014.
31. Barber JR. Contact mechanics. Berlin: Springer International Publishing; 2018.
32. ANSI/AGMA 2101-C95. Fundamental rating factors and calculation methods for involute spur and helical gear teeth. 1997.
33. Spitas V, Papadopoulos GA, Spitas C, Costopoulos T. Experimental investigation of load sharing in multiple gear tooth contact using the stress-optical method of caustics. Strain. 2011;47:227–33. doi:10.1111/j.1475-1305.2008.00558.x.

34. Zhang XG, Xie YC, Wang PF. A forming method and theoretical verification of curvilinear cylindrical gears for adjustable contact area. J Mech Trans. 2021;46(7):38–44.
35. Zhang X, Liang Z. Mathematical model and contact characteristics of curvilinear cylindrical gears with line contact. J Braz Soc Mech Sci Eng. 2021;43(4):1–18. doi:10.1007/s40430-021-02894-w.